Nanoscale

RSC Publishing

PAPER

View Article Online
View Journal | View Issue

Cite this: *Nanoscale*, 2013, **5**, 10360

Multiplex acute leukemia cytosensing using multifunctional hybrid electrochemical nanoprobes at a hierarchically nanoarchitectured electrode interface†

Tingting Zheng,[ab] Tingting Tan,[c] Qingfeng Zhang,[b] Jia-Ju Fu,[a] Jia-Jun Wu,[a] Kui Zhang,[c] Jun-Jie Zhu*[a] and Hui Wang*[b]

We have developed a robust, nanobiotechnology-based electrochemical cytosensing approach with high sensitivity, selectivity, and reproducibility toward the simultaneous multiplex detection and classification of both acute myeloid leukemia and acute lymphocytic leukemia cells. The construction of the electrochemical cytosensor involves the hierarchical assembly of dual aptamer-functionalized, multilayered graphene–Au nanoparticle electrode interface and the utilization of hybrid electrochemical nanoprobes co-functionalized with redox tags, horseradish peroxidase, and cell-targeting nucleic acid aptamers. The hybrid nanoprobes are multifunctional, capable of specifically targeting the cells of interest, amplifying the electrochemical signals, and generating distinguishable signals for multiplex cytosensing. The as-assembled electrode interface not only greatly facilitates the interfacial electron transfer process due to its high conductivity and surface area but also exhibits excellent biocompatibility and specificity for cell recognition and adhesion. A superstructured sandwich-type sensor geometry is adopted for electrochemical cytosensing, with the cells of interest sandwiched between the nanoprobes and the electrode interface. Such an electrochemical sensing strategy allows for ultrasensitive, multiplex acute leukemia cytosensing with a detection limit as low as ~350 cells per mL and a wide linear response range from 5×10^2 to 1×10^7 cells per mL for HL-60 and CEM cells, with minimal cross-reactivity and interference from non-targeting cells. This electrochemical cytosensing approach holds great promise as a new point-of-care diagnostic tool for early detection and classification of human acute leukemia and may be readily expanded to multiplex cytosensing of other cancer cells.

Received 4th June 2013
Accepted 12th August 2013

DOI: 10.1039/c3nr02903d

www.rsc.org/nanoscale

Introduction

The past two decades have witnessed significant progress in the development of robust analytical tools with high sensitivity, selectivity, and reproducibility toward early diagnosis of cancer.[1–4] Electrochemical cytosensing has emerged as an extremely attractive method that can be readily implemented into quantitative bioassays for high-throughput clinical applications.[5–9] Utilization of rationally designed multifunctional nanoprobes and specifically tailored nano-biointerfaces for electrochemical cytosensing provides unique opportunities to optimize the interfacial electron transfer and cell recognition processes, allowing for the integration of large signal amplification, enhanced detection specificity, and expanded multiplex sensing capabilities on a cytosensor. In this paper, we demonstrate that by combining simple electrochemical transducers with multifunctional hybrid nanoprobes and hierarchically nanoarchitectured electrode interface, a highly sensitive and selective electrochemical cytosensing platform can be developed for the simultaneous detection of both acute myeloid leukemia (AML) and acute lymphocytic leukemia (ALL) cells.

Leukemia is a type of fatal cancer that affects the bone marrow, the blood cells, and other parts of the lymphatic system.[10] Early detection of acute leukemia is of vital importance because acute leukemia causes a large number of abnormal blood cells to be produced and subsequently invade the bloodstream much more rapidly than chronic leukemia.[11] Acute leukemia is divided into two main types, AML and ALL.[12,13] The American Cancer Society has estimated about 14 590 new cases of AML and 6070 new cases of ALL with 10 370 and 1430 expected deaths from AML and ALL, respectively, in the United States in 2013.[14,15] Identifying the specific type and quantifying the progression level of acute leukemia at the early

[a]*State Key Laboratory of Analytical Chemistry for Life Science, School of Chemistry and Chemical Engineering, Nanjing University, Nanjing, Jiangsu 210093, China. E-mail: jjzhu@nju.edu.cn*

[b]*Department of Chemistry and Biochemistry, University of South Carolina, 631 Sumter Street, Columbia, South Carolina 29208, USA. E-mail: wang344@mailbox.sc.edu*

[c]*Department of Medical Laboratory, The Affiliated Drum Tower Hospital of Nanjing University Medical School, Nanjing, Jiangsu 210008, China*

† Electronic supplementary information (ESI) available: Additional figures as noted in the text. See DOI: 10.1039/c3nr02903d

stage are of paramount importance for the doctors to better predict each patient's prognosis and select the most appropriate treatment accordingly. The diagnosis of acute leukemia is typically performed in blood samples taken from vein or bone marrow samples obtained from aspiration or needle biopsy.[16] A variety of analytical tools have been developed for acute leukemia diagnosis, such as the complete blood count and peripheral blood smear,[17,18] cytochemistry test,[19–21] immunophenotyping by flow cytometry[22–25] or microarrays,[26,27] and polymerase chain reaction (PCR)-based DNA tests.[28–31] These methods either require time-consuming sample preparation procedures and/or sophisticated instrumentation or involve tedious data collection/analysis processes, limiting their use as point-of-care diagnostic tools. The amplification of malignant cell mutations by PCR may even lead to false-negative results in some cases.[32] Therefore there is an urgent need to develop a robust preliminary testing approach, which can provide more accurate and quantitative diagnostic results in a timely manner for the early detection and classification of acute leukemia.

Here we have developed a nanobiotechnology-based electrochemical approach with unique advantages of operational simplicity, low cost, high sensitivity, excellent selectivity, and ease of miniaturization toward multiplex acute leukemia cytosensing. Using HL-60 and CEM as representative model AML and ALL cells respectively, we demonstrate the construction of a multicellular electrochemical cytosensing platform that simultaneously detects both AML and ALL cells in a highly quantitative manner. The high detection sensitivity and selectivity, integrated with the multiplex sensing capabilities, are achieved essentially by hierarchically assembling dual aptamer-functionalized graphene–Au multilayered nanostructures on a glassy carbon electrode surface and using hybrid electrochemical nanoprobes co-functionalized with distinguishable redox tags, signal amplifying enzyme, and cell-targeting aptamers. This multiplex electrochemical cytosensing approach is of great clinical value for the high throughput early detection and classification of human acute leukemia.

Experimental details

Materials and chemicals

Tris(2-carboxyethyl)phosphine hydrochloride (TCEP) was purchased from Bio. Basic Inc. (Markham Ontario, Canada). Tetrachloroauric acid ($HAuCl_4 \cdot 4H_2O$), trisodium citrate and tetraethoxysilane (TEOS), pluronic P123, thionin acetate salt, anthraquinone, calcein-AM, and 6-mercapto-1-hexanol (MCH) were all purchased from Sigma-Aldrich (St. Louis, USA). DiI was purchased from Beyotime Institute of Biotechnology (Nantong, China). Trypan blue and horseradish peroxidase (HRP) were purchased from Beijing Biosynthesis Biotechnology Co. Ltd. (Beijing, China). Phosphate buffer saline (PBS, 0.01 M, pH 7.4) contained 136.7 mM NaCl, 2.7 mM KCl, 8.7 mM Na_2HPO_4, and 1.4 mM KH_2PO_4. All reagents were of analytical grade and were used without further purification. Ultra-pure water (18.2 MΩ resistivity, Milli-Q, Millipore) was used for all the experiments. Thiolated aptamers were synthesized and purified by Shanghai Sangon Biotechnology Co. Ltd. (Shanghai, China). The sequence of the sgc8c aptamer was 5′-HS-ATC TAA CTG CTG CGC CGC CGG GAA AAT ACT GTA CGG TTA GA-3′. The sequence of the KH1C12 aptamer was 5′-HS-ATC CAG AGT GAC GCA GCA TGC CCT AGT TAC TAC TAC TCT TTT TAG CAA ACG CCC TCG CTT TGG ACA CGG TGG CTT AGT-3′.

Apparatus

UV-vis extinction spectra were recorded on a UV-3600 spectrophotometer (Shimadzu, Kyoto, Japan). Powder X-ray diffraction (XRD) patterns were performed using a Philip-X'Pert X-ray diffractometer with a Cu Kα X-ray source, $\lambda = 0.15418$ nm. Scanning electron micrographs (SEM) were obtained with a Hitachi S4800 scanning electron microscope. Transmission electron micrographs (TEM) were measured on a JEOLJEM 200CX transmission electron microscope using an accelerating voltage of 200 kV. Confocal laser scanning microscopy (CLSM) studies were performed using a Leica TCS SP5 fluorescence microscope (Germany). Electrochemical impedance spectroscopy (EIS) was performed with an Autolab electrochemical analyzer (Eco Chemie, The Netherlands) in a 10 mM $K_3Fe(CN)_6$/$K_4Fe(CN)_6$ (1 : 1) mixture with 1.0 M KCl as the supporting electrolyte, using an alternating current voltage of 5.0 mV, within the frequency range of 0.1–10 kHz. Cyclic voltammetry (CV) and differential pulse voltammetry (DPV) measurements were performed on a CHI 660C electrochemical workstation using a three-electrode system.

Nanoprobe fabrication

Mesoporous SBA-15 was prepared following a previously reported protocol.[33] Briefly, 3 g of Pluronic P123 and 8.5 g of TEOS were dissolved in 120 mL of 1.5 M HCl aqueous solution and stirred at 35 °C for 20 h. The solution was then moved into an autoclave and aged at 120 °C for 24 h. The precipitate was washed with H_2O and ethanol, and dried at room temperature in air. The as-synthesized SBA-15 sample was calcined by slowly increasing the temperature from 25 °C to 500 °C over 8 h and then remained at 500 °C for 6 h.

The thionine modified SBA-15 (SBA-15/Thi) was fabricated by dispersing 10.0 mg of SBA-15 in 1.0 mL of H_2O, followed by addition of 2.0 mL of saturated thionine solution. The mixture was sonicated for 20 min and centrifuged at 6000 rpm for 10 min to obtain the precipitate of SBA-15/Thi. The precipitate was washed several times with H_2O and redispersed in 1.0 mL 2-(*N*-morpholino)ethanesulfonic acid (MES) buffer (pH 5.2). Colloidal Au NPs, which were prepared by the reduction of $HAuCl_4$ with trisodium citrate,[34] were mixed with SBA-15/Thi, sonicated for 30 min, centrifuged at 6000 rpm, and redispersed in H_2O. Then, 50 μL of HRP (1 mg mL^{-1}) and 50 μL of thiolated Sgc8c aptamer (HS-Sgc8c, 5 μM) were added into the dispersion. After incubation at 25 °C under shaking for 4 h and keeping overnight at 4 °C, the precipitate was isolated by centrifugation at 6000 rpm for 10 min to remove the nonconjugated HRP and aptamer. The HRP-Sgc8c-SBA-15/Thi/Au NP hybrid nanoprobes were obtained by redispersing the precipitate in an incubation buffer containing 1 mM Ca^{2+}, 1 mM Mn^{2+} and 0.1% BSA and stored at 4 °C. HRP-KH1C12-SBA-15/AQ/Au NP nanoprobes were

fabricated following the same protocol except that anthraquinone was used instead of thionine.

Cytosensor assembly

A glassy carbon electrode (GCE, 3 mm diameter) was polished to a mirror using 0.3 and 0.05 μm alumina slurry (Buehler) followed by rinsing thoroughly with H_2O. After successive sonication in 1 : 1 nitric acid and acetone, the electrode was rinsed with H_2O and allowed to dry at room temperature. For electrodeposition of Au NP–EG nanocomposite films, a dispersion containing 1.0 mg mL^{-1} graphene oxide (GO) and 100 mM $HAuCl_4$ was prepared. The cyclic voltammetric reduction was performed in the deposition solutions with magnetic stirring and N_2 bubbling on a CHI 660C electrochemical workstation (CH Instruments, Shanghai) using a three-electrode system: the prepared GCE as the working electrode, Pt foil as the counter electrode, and an SCE as the reference electrode. The scan was performed between −1.5 and 0.6 V at a rate of 25 mV s^{-1}. After deposition, the working electrode was rinsed with H_2O. Then, 5 μL of SH-KH1C12 (5 μM) and SH-Sgc8c (5 μM) 1 : 1 volume ratio mixture was immediately applied to the Au NP–EG-modified GCE and incubated at 4 °C overnight. After incubation, the aptamer/Au NP–EG/GCE was rinsed with PBS (pH 7.4) carefully, immersed in 60 μL of 2 mM MCH for 1 h at room temperature to block the nonspecific binding sites, and then washed with PBS (pH 7.4) thoroughly.

The dual aptamer-functionalized, Au NP–EG modified GCE was soaked in 100 μL of cell suspension at a certain concentration and incubated at 37 °C for 1 h to capture the cells. Then the electrode was taken out and rinsed with incubation buffer to remove the noncaptured cells. Finally, 10 μL of an equivalent mixture of HRP-KH1C12-SBA-15/AQ/Au and HRP-Sgc8c-SBA-15/Thi/Au nanoprobes was dropped onto the electrode surface for 1 h at 37 °C. Before electrochemical measurements, the cytosensor was washed thoroughly with the incubation buffer to remove nonspecifically bound nanoprobes to minimize the background response. For cytosensing, the electrode was placed in a glass cell containing 1 mM H_2O_2–PBS (pH 6.5) and connected to a CHI 660C electrochemical workstation. DPV measurements were performed from 50 mV to −700 mV (*vs.* Ag/AgCl) with a pulse amplitude of 50 mV and a pulse width of 50 ms.

Cell lines and cell culture

HL-60, CEM, K562 and Hela cells were obtained from Nanjing KeyGen Biotech Co., Ltd. and cultured in a flask in RPMI 1640 medium (Gibco, Grand Island, NY) supplemented with 10% fetal calf serum (FCS, Sigma), penicillin (100 μg mL^{-1}) and streptomycin (100 μg mL^{-1}) in an incubator (5% CO_2, 37 °C). At the logarithmic growth phase, the cells were collected and separated from the medium by centrifugation at 1000 rpm for 2 min and then resuspended in the binding buffer (4.5 g L^{-1} glucose, 5 mM $MgCl_2$, 0.1 mg mL^{-1} tRNA and 1 mg mL^{-1} BSA, all dissolved in Dulbecco's phosphate-buffer saline with $CaCl_2$ and $MgCl_2$) to obtain a homogeneous cell suspension. The binding buffer was used to ensure the effective binding affinity between cells and aptamers. Red blood cells were obtained by centrifugation from whole blood samples provided by Nanjing Drum Tower Hospital.

Results and discussion

Fabrication of multifunctional nanoprobes

The multifunctional electrochemical nanoprobes were fabricated through a layer-by-layer (LBL) assembly process, which is schematically illustrated in Fig. 1A. The as-fabricated hybrid nanoprobes have a unique set of combined capabilities of multiplex cytosensing, specific cell targeting, and enzyme-catalyzed signal amplification. By using anthraquinone (AQ) and thionine (Thi) as two distinguishable redox-tags, multiplex sensing capability can be achieved by generating amperometric signals at distinctly different potentials. The amperometric peak currents and the peak positions can be used to quantify the concentration and identify the type of leukemia cells, respectively. The horseradish peroxidase (HRP) immobilized on the nanoprobes dramatically amplifies the electrochemical signals due to the HRP-catalyzed oxidation of the redox-tags by H_2O_2. Such enzyme-catalyzed redox processes generated significantly enhanced amperometric responses than the direct electrochemical signals from the redox tags.[35] The functionalization of the nanoprobes with cell-targeting aptamers (KH1C12

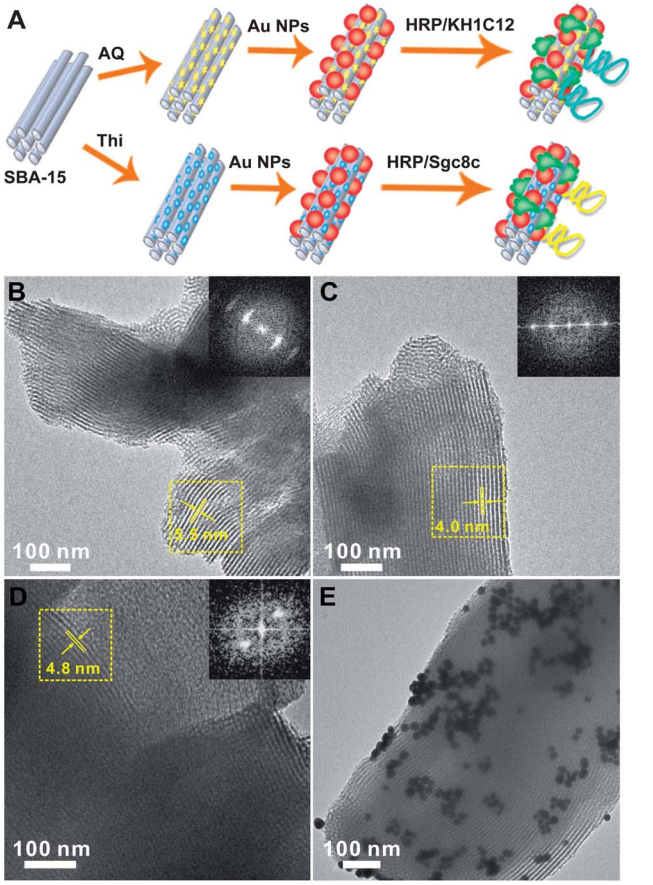

Fig. 1 (A) Schemes illustrating the LBL assembly processes for the fabrication of SBA-15/redox-tags/Au NP/HRP/aptamer hybrid electrochemical nanoprobes. The relative sizes of the SBA-15, redox tags, Au NPs, HRP, and aptamers are not to scale. TEM images of SBA-15 (B) before redox tag loading and after loading of (C) Thi and (D) AQ. The insets show the Fourier Transform patterns obtained from the selected regions in the TEM images. (E) TEM image of SBA-15 loaded with Thi and decorated with Au NPs.

aptamer for HL-60 cell recognition[36] and Sgc8c aptamer for CEM cell recognition[37]) allows for the selective attachment of the nanoprobes onto the surface of the specific targeting cells. Nucleic acid aptamers, which have been recently identified as specific ligands for cell surface biomarkers, have the unique capability of recognizing trace cancer cells from complex living samples.[38,39] The identification of specific aptamers for leukemia cell recognition opens up unique opportunities for the development of new methods for leukemia diagnosis and new drugs for leukemia therapy.[36,40]

SBA-15,[41] a mesoporous nanostructure of silica, was used as the carrier to load a large amount of redox-tags, which generated the electrochemical signals for cytosensing. The adsorption of AQ and Thi on the wall surfaces of SBA-15 resulted in the decrease of the apparent pore diameters, which was clearly visualized in the transmission electron microscopy (TEM) images shown in Fig. 1B–D. The average pore sizes of SBA-15 were measured to be ~5.5 nm prior to redox-tag loading, ~4.0 nm after loading of Thi, and ~4.8 nm after loading of AQ, respectively. The periodicity of SBA-15, however, remained at ~10.1 nm and was essentially unaffected by the loading of the redox-tags, as shown by both TEM images (Fig. 1B–D) and the corresponding Fourier Transform patterns obtained from the images (insets of Fig. 1B–D). The outer surfaces of the SBA-15 loaded with Thi or AQ were then decorated with a sub-monolayer of Au nanoparticles (NPs) (see the TEM image in Fig. 1E) through electrostatic interactions.

The structures of SBA-15 and the as-assembled SBA-15/AQ/Au and SBA-15/Thi/Au nanocomposites were further characterized by powder X-ray diffraction (XRD) measurements. The small-angle XRD patterns shown in Fig. 2A further verified that the hexagonally packed mesoporous structures and the structural periodicity of SBA-15 were well-maintained in the redox-tag loading processes. The silica framework of SBA-15 was amorphous as only a broad feature was observed in the wide-angle XRD pattern (see pattern a in Fig. 2B). After attaching Au NPs onto the surface of SBA-15 (see pattern b in Fig. 2B), a series of diffraction peaks corresponding to the (111), (200), (220) and (311) planes of the cubic phase Au nanocrystals[42] were clearly observed on top of the signals from SBA-15. The last step in the nanoprobe fabrication was the co-functionalization of the surfaces of the attached Au NPs with HRP and thiolated KH1C12 or Sgc8c aptamer through Au-thiol interactions. The hybrid nanoprobe assembly processes were monitored by microeletrophoresis measurements whose results were expressed as ζ-potentials as shown in Fig. S1 in the ESI.† SBA-15 was negatively charged at neutral pH due to the presence of hydroxyl groups on its surfaces. Since both AQ and Thi were positively charged in weakly acidic solution,[43] the adsorption of the redox-tag layers onto the SBA-15 surfaces yielded positive ζ-potentials. The subsequent attachment of negatively charged Au NPs onto the outer surfaces of SBA-15 switched the ζ-potentials back to negative values. The evolution of the ζ-potentials clearly verified that the hybrid nanoporbes were fabricated essentially through stepwise LBL assembly processes.

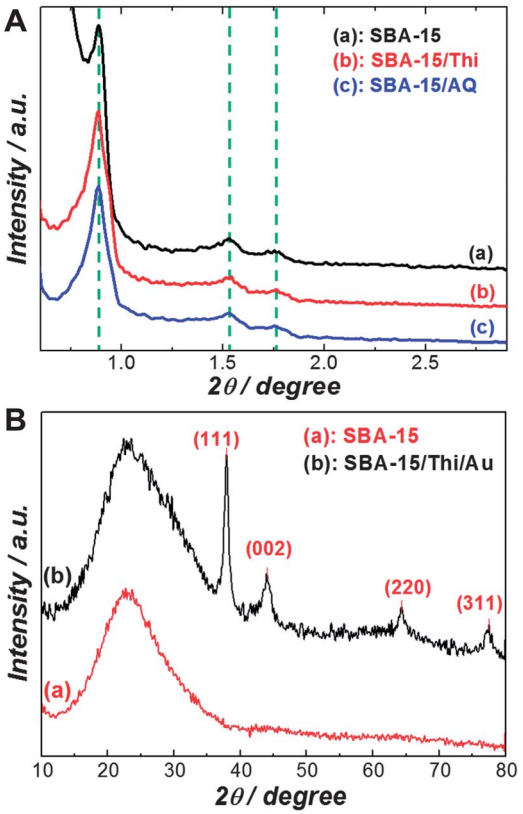

Fig. 2 (A) Small angle XRD patterns of SBA-15, SBA-15 loaded with Thi, and SBA-15 loaded with AQ. (B) Wide-angle XRD patterns of SBA-15 and SBA-15/Thi/Au nanocomposites.

Assembly of electrochemical cytosensors

Fig. 3 schematically illustrates the major steps involved in the cytosensor assembly process. To increase the surface area and conductivity of the cytosensing interface, we first modified the GCE surface with a multilayered Au NP–graphene composite film. Then thiolated cell targeting aptamers, SH-KH1C12 and SH-Sgc8c, were both conjugated to the Au NPs in the composite film through Au–thiol interactions to create a biocompatible

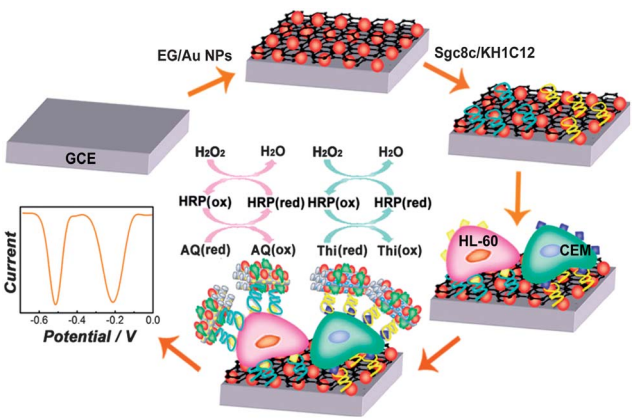

Fig. 3 Schemes illustrating the major steps involved in the construction of the electrochemical cytosensor.

interface for specific capture of both HL-60 and CEM cells. Finally, after the targeting cells were captured on the electrode surface, the hybrid nanoprobes were further tethered onto the surfaces of the captured cells. In this way, a sandwich-like superstructure was assembled with the leukemia cells of interest sandwiched between the electrode interface and the electrochemical nanoprobes.

We adopted a co-electrodeposition method to hierarchically assemble a multilayered Au NP–graphene composite film on the GCE surface.[44] It was recently reported that colloidal graphene oxide (GO) could be electrochemically reduced to yield multilayered graphene films on an electrode surface by cyclic voltammetry (CV).[45] A typical CV diagram of GO electrolysis on a GCE is shown in Fig. S2 in the ESI.† The cathodic peak I was attributed to the irreversible electrochemical reduction of GO while the cathodic peak II and the anodic peak III were ascribed to the redox pair of some oxygen-containing groups on the graphene plane.[45] The progressive increase of the peak currents with successive potential scans indicated layer-by-layer surface deposition of graphene onto the GCE. As shown in Fig. 4A, the CV diagram for the electrolysis of GO coexisting with $HAuCl_4$ displays dramatically different features from those of GO electrolysis. The deposition potential of Au NPs (−0.25 V *vs.* SCE) was much lower than that of graphene (−1.2 V *vs.* SCE). As a result, the Au NPs and electrochemically reduced graphene (EG) were alternately deposited layer by layer during the repeated cyclic voltammetric scans, leading to the formation of hierarchically multilayered nanostructures consisting of alternating layers of Au NPs and EG sheets.[44] Cyclic voltammetric scans with a scan rate of 25 mV s^{-1} at room temperature in the voltage range of −1.5 V to 0.6 V allowed for complete and homogenous deposition of both Au NPs and EG in each scan cycle, which was consistent with previous observation.[44] Fig. 4B reveals that Au NPs with an average diameter of ~15 nm were uniformly distributed between the thin and transparent graphene sheets. The reduction currents progressively increased with successive scan cycles and were remarkably larger than those of GO electrolysis. This is because the intercalation of highly conductive Au NPs between graphene sheets greatly improved the conductivity of the nanocomposite film and further increased the surface area by effectively preventing graphene agglomeration.[44] Fig. S3 in the ESI† shows the UV-visible extinction spectra of GO and the electrochemically deposited Au NP–EG composite film. Colloidal GO suspension showed an absorption peak at 229 nm, while reduction of GO into graphene resulted in a red-shift of this absorption peak to 268 nm, indicating the formation of graphene.[46] The extinction peak at 532 nm was the plasmon resonance band of the Au NPs in the nanocomposite film. The wide angle XRD patterns of the GO and Au NP–EG hybrid film are shown in Fig. S4 in the ESI.† The characteristic XRD peak of GO centered at 9.12° completely disappeared after the electrodeposition, strongly indicating that GO was electrochemically reduced into graphene.[47] A series of characteristic diffraction peaks corresponding to the cubic phase of Au[42] were clearly observed in the XRD pattern of the Au–EG hybrid film, further verifying the co-deposition of EG and Au NPs on the GCE surface.

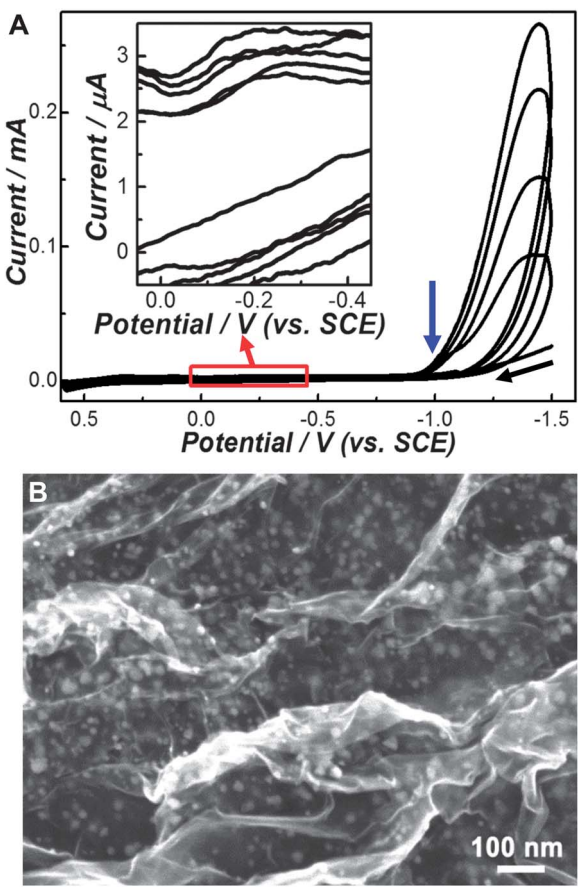

Fig. 4 (A) Cyclic voltammograms for the electrolysis of 1.0 mg mL^{-1} GO + 100 mM $HAuCl_4$ in pH 9.0 carbonate buffer solution at a scan rate of 25 mV s^{-1}. (B) SEM image of the electrochemically deposited Au NP–EG multilayered composite film on the GCE.

The surface modification of the GCE with the Au NP–EG nanocomposite films effectively facilitated the interfacial electron transfer process. $[Fe(CN)_6]^{3-}/[Fe(CN)_6]^{4-}$ was used as the redox probe to characterize the electron transfer resistivity of the bare and modified GCEs. As shown in Fig. S5 in the ESI,† the CV peak currents became increasingly more intense as the number of layers in the Au NP–EG composite films increased. Optimal electrochemical response was obtained when 4 layers of EG were electrochemically deposited onto the GCE surface. Although deposition of more layers of EG and Au NPs resulted in larger peak currents, the background currents also significantly increased largely due to the increase in interfacial areas. Therefore, in the process of cytosensor assembly, we carried out the electrodeposition through 5 cycles of CV scans and stopped at −1.0 V in the fifth scan cycle (indicated by a blue arrow in Fig. 4A) such that 4 alternating layers of Au NPs and EG were deposited on the GCE surface with an additional sub-monolayer of Au NPs deposited on the upper surface of the top layer of EG. The Au NPs on the top layer were then functionalized with thiolated aptamers, SH-KH1C12 and SH-Sgc8c, to selectively capture both HL-60 and CEM cells, respectively. The nonspecific cell binding sites were effectively blocked using 6-mercapto-1-hexanol (MCH).

We used confocal fluorescence microscopy to characterize the adhesion specificity and viability of the leukemia cells captured at the as-assembled electrode interface. To distinguish the two types of leukemia cells, the CEM and HL-60 cells were stained with trypan blue and DiI, respectively, and then captured on the electrode surface. As shown in Fig. 5A and B, strong blue and red fluorescent signals were observed from trypan blue-stained CEM cells and DiI-stained HL-60 cells under 375 nm and 549 nm laser excitations, respectively, indicating that both CEM and HL-60 cells were selectively captured on the electrode surface. To visualize whether the cells were still alive on the electrode surface, the captured cells were stained with calcein acetoxymethyl ester (calcein-AM), a widely used cell viability fluorescence indicator. Strong green fluorescence (excited at 488 nm) from both CEM and HL-60 cells (Fig. 5C) was observed and the cell distribution pattern was almost identical to that of the overlaid image of Fig. 5A and B (Fig. 5D), indicating that the dual aptamer functionalized, Au NP–EG modified electrode interface exhibited excellent biocompatibility to both CEM and HL-60 cells. More than 95% of the CEM and HL-60 cells captured on the electrode interface were observed to be alive in RPMI 1640 medium for over 48 h.

The stepwise cytosensor assembly process was monitored by electrochemical impedance spectroscopy (EIS) measurements. The electron-transfer resistance (R_{et}) of the redox probe, $[Fe(CN)_6]^{3-}/[Fe(CN)_6]^{4-}$, at a GCE was measured at multiple stages during the cytosensor assembly process and the resulting Nyquist plots are shown in Fig. 6. The EIS results were fitted to a Randles equivalent circuit (inset in Fig. 6), which included the solution resistance (R_s), R_{et} of $[Fe(CN)_6]^{3-}/[Fe(CN)_6]^{4-}$, the constant phase element (C_{dl}), and Warburg impedance (W). In the Nyquist diagrams, the diameters of the semicircles reflected the R_{et} of redox conversion of the electroactive marker $[Fe(CN)_6]^{3-}/[Fe(CN)_6]^{4-}$ on the GCE at certain applied potentials. It was observed that the assembly of the Au NP–EG nanocomposite layers on the GCE surface resulted in a substantial decrease in the R_{et} because the Au NP–EG nanocomposite film significantly increased the surface area and electro-conductivity of the electrode interface and thus facilitated the interfacial electron transfer process. After aptamer-functionalization and subsequent MCH blocking, the electron transfer resistance significantly increased due to the fact that the aptamers acted as an inert blocking layer that hindered the electron transfer. The subsequent adhesion of cells onto the electrode interface further obstructed the access of the redox probes to the electrode, leading to a substantially higher R_{et} value. Finally, the attachment of the hybrid nanoprobes onto the cell surfaces further increased the R_{et} essentially due to the barrier effect of SBA-15 against the electron communication between $[Fe(CN)_6]^{3-}/[Fe(CN)_6]^{4-}$ and the electrode surface. The evolution of the R_{et} during the cytosensor assembly process is shown in Fig. S6 in the ESI.† The standard deviations, which are shown as the error bars in Fig. S6,† were obtained from independent EIS measurements performed on three cytosensors.

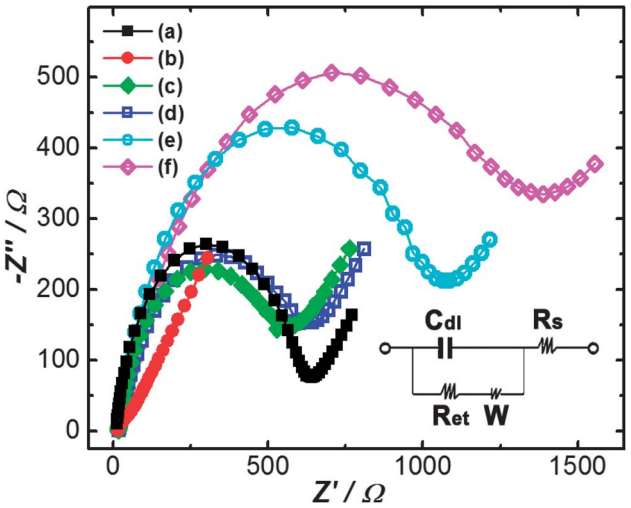

Fig. 6 Nyquist diagrams of electrochemical impedance spectra recorded from 0.1 to 10^6 Hz for $[Fe(CN)_6]^{3-}/[Fe(CN)_6]^{4-}$ (10 mM, 1 : 1) in 1.0 M KCl at a bare GCE (a), Au NP–EG/GCE (b), aptamer/Au NP–EG/GCE (c), MCH/aptamer/Au NP–EG/GCE (d), cell/MCH/aptamer/Au NP–EG/GCE (e), nanoprobes/cell/MCH/aptamer/Au NP–EG/GCE (f). The inset shows the equivalent circuit used to fit the EIS data.

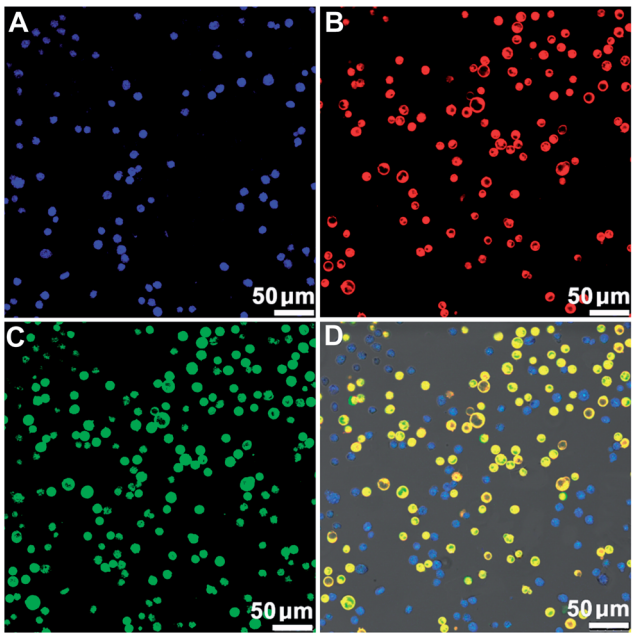

Fig. 5 Fluorescence microscopy images of (A) CEM cells stained by trypan blue, (B) HL-60 cells stained by DiI, and (C) both captured CEM and HL-60 cells stained by calcein-AM after cell capture on the ITO/Au NP–EG/aptamer electrode for 1 h, and (D) the overlaid image of the fluorescent signals from all captured cells.

Electrochemical cytosensing

The detection sensitivity and linear response range of the multiplexed cytosensor were evaluated using HL-60 and CEM cells as the targeting cells. Differential pulse voltammetric (DPV) measurements were carried out in phosphate buffered saline (PBS) at pH 6.5 containing 1 mM of H_2O_2 after incubating the dual aptamer functionalized, Au NP–EG modified GCE with the targeting cells at various concentration levels and the

electrochemical nanoprobes. As shown in Fig. 7A, the DPV reduction currents progressively increased with the HL-60 and CEM cell concentrations. The calibration plots for both HL-60 and CEM cells displayed a good linear relationship between the reduction peak current and the logarithm of the cell concentration in the range of 5×10^2–1×10^7 cells per mL with correlation coefficients of 0.994 and 0.996 for HL-60 and CEM cells ($n = 10$), respectively (Fig. 7B). The error bars in Fig. 7B represent the standard deviations obtained from parallel measurements performed using five different cytosensors. The detection limits for HL-60 and CEM cells were determined to be ~350 cells per mL at 3σ, which were lower than those of previous reported EIS-based cytosensing approaches.[48,49] The high detection sensitivity may be a consequence of the synergistic effects of excellent conductivity of Au NP–EG nanocomposite films, the loading of a large amount of redox-tags in SBA-15, and the high catalytic activity of HRP toward H_2O_2 reduction. The wide linear response ranges allow for the quantification of both types of acute leukemia cells over a broad distribution of concentration levels.

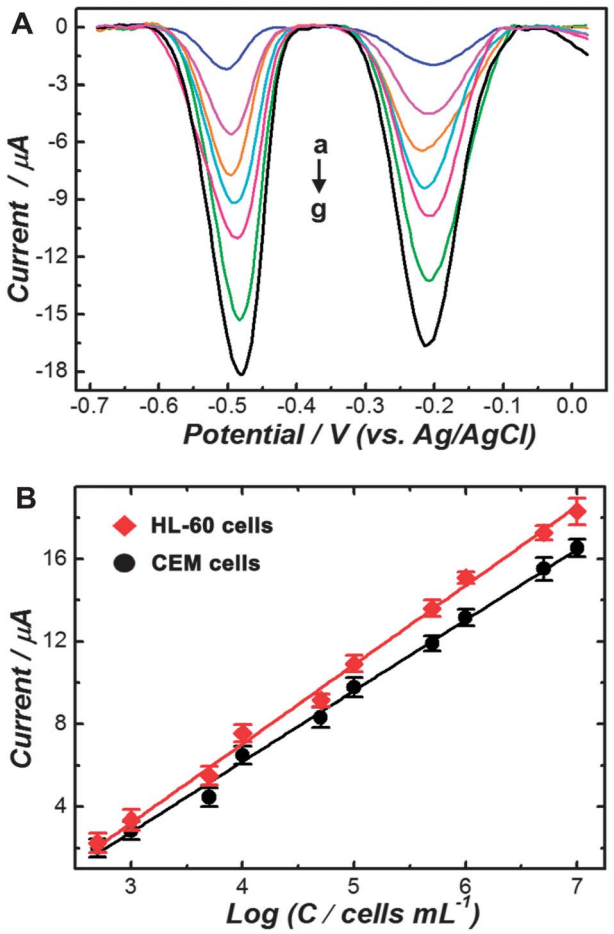

Fig. 7 (A) DPV responses at different HL-60 and CEM cell concentrations (from curve a to g: 5×10^2, 5×10^3, 1×10^4, 5×10^4, 1×10^5, 1×10^6 and 1×10^7 cells per mL of HL-60 and CEM cells, respectively). (B) Calibration curves for HL-60 and CEM cells in PBS, pH 6.5, containing 1 mM H_2O_2.

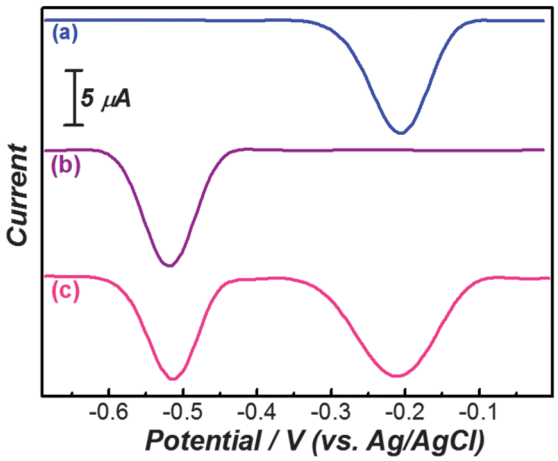

Fig. 8 DPV signals for the investigation of cross-reactivity: (a) 1×10^5 cells per mL CEM solution, (b) 1×10^5 cells per mL HL-60 solution, and (c) a mixture solution containing 1×10^5 cells per mL HL-60 and 1×10^5 cells per mL CEM.

An excellent multiplexed cytosensor must exclude cross-reactivity between different types of targeting cells. The cross-reactivity of the as-fabricated cytosensors was evaluated by comparing the amperometric responses obtained in the presence of both HL-60 and CEM cells to the electrochemical signals obtained with only one type of cells present. Fig. 8 shows the results of a typical electrochemical assay, in which the dual-aptamer modified electrode was incubated with 10^5 cells per mL of CEM cells (curve a), 10^5 cells per mL of HL-60 cells (curve b), and a mixture of 10^5 cells per mL of CEM cells and 10^5 cells per mL HL-60 cells (curve c), followed by incubation with the hybrid nanoprobes (SBA-15/AQ/Au NP-KH1C12-HRP and SBA-15/Thi/Au NP-Sgc8c-HRP). When only CEM cells were present, a well-defined DPV peak was obtained at −0.204 V *vs.* Ag/AgCl (electrochemical signal from Thi), while in the presence of HL-60 cells only, a single DPV peak at −0.518 V *vs.* Ag/AgCl (electrochemical signal from AQ) was observed. The two peaks were used to quantify the concentrations of CEM and HL-60 cells, respectively. When both cells were incubated, two signal peaks appeared simultaneously in the DPV diagrams and the detection of CEM and HL-60 cells showed minimal interference with each other.

The detection specificity is also a key issue in cytosensing. In this work, Hela (a non-leukemia cancer cell line), K562 (a chronic leukemia cell line), and normal red blood cells were used as interferences to evaluate the selectivity of the cytosensor. In Fig. 9, the electrochemical signals of 10^5 cells per mL of HL-60 and 10^5 cells per mL of CEM cells in the absence of interference are compared with those obtained in the presence of interference cells at 10^6 cells per mL concentration level. It was apparent that the presence of various non-targeting cells, even at concentrations an order of magnitude higher than the targeting cells, had minimal interfering effects on the electrochemical detection. These results clearly indicated that the as-constructed electrochemical cytosensor had excellent sensing specificity and was capable of differentiating HL-60 and CEM cells from complex samples.

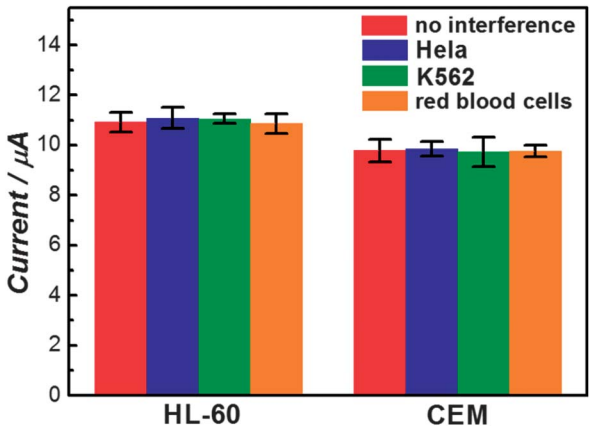

Fig. 9 DPV responses at the concentration of 1×10^5 cells per mL HL-60 and 1×10^5 cells per mL CEM in the absence of interfering cells and in the presence of 1×10^6 cells per mL of Hela, 1×10^6 cells per mL of K562, and 1×10^6 cells per mL of red blood cells. The error bars represent the standard deviation obtained from measurements performed on the three cytosensors.

Conclusions

Taking the advantage of novel nanobiotechnology, a multiplex electrochemical cytosensing platform has been constructed to simultaneously detect and classify both AML and ALL cells in a highly sensitive, selective, and reproducible manner. The multifunctional hybrid nanoprobes integrate unique capabilities to specifically target the cells of interest, to amplify the electrochemical signals, and to generate distinguishable signals for multiplex cytosensing. The hierarchical assembly of Au NP–graphene multiplayer composite films and dual aptamer functionalization on the GCE surface provide not only a highly conductive and biocompatible electrode interface for electrochemical sensing but also an analogue of extracellular matrix for the specific cell recognition and adhesion. The as-fabricated cytosensors showed a detection limit of ~350 cells per mL and exhibited a wide linear response range of 5×10^2–1×10^7 cells per mL for both HL-60 and CEM cells, with minimal cross-reactivity and interference from non-targeting cells. This robust electrochemical cytosensing approach is believed to be of great clinical value as a diagnostic tool for early detection and classification of human acute leukemia. By selecting the nucleic acid aptamers that specifically target other types of cancer cells,[50–52] this approach can be readily expanded to multiplex detection and classification of a variety of cancer cells.

Acknowledgements

T. Z. acknowledges the Fellowship for Oversea Visiting Students provided by the Chinese Scholarship Council, Ministry of Education of China. J.-J. Z. acknowledges the funding provided by National Basic Research Program of China (Grant 2011CB933502) and the National Natural Science Foundation of China (21020102038, 21121091). H. W. acknowledges the support by University of South Carolina New Faculty Start-up Funds and United States National Science Foundation CAREER Award (DMR-1253231).

Notes and references

1 M. Ferrari, *Nat. Rev. Cancer*, 2005, **5**, 161–171.
2 S. Nagrath, L. V. Sequist, S. Maheswaran, D. W. Bell, D. Irimia, L. Ulkus, M. R. Smith, E. L. Kwak, S. Digumarthy, A. Muzikansky, P. Ryan, U. J. Balis, R. G. Tompkins, D. A. Haber and M. Toner, *Nature*, 2007, **450**, 1235–1239.
3 D. Sidransky, *Science*, 1997, **278**, 1054–1058.
4 I. E. Tothill, *Semin. Cell Dev. Biol.*, 2009, **20**, 55–62.
5 W. Cheng, L. Ding, J. P. Lei, S. J. Ding and H. X. Ju, *Anal. Chem.*, 2008, **80**, 3867–3872.
6 J. Y. Liu, Y. N. Qin, D. Li, T. S. Wang, Y. Q. Liu, J. Wang and E. K. Wang, *Biosens. Bioelectron.*, 2013, **41**, 436–441.
7 B. Zhou, X. L. Xiao, L. L. Xu, L. Zhu, L. Tan, H. Tang, Y. Y. Zhang, Q. J. Xie and S. Z. Yao, *Biosens. Bioelectron.*, 2012, **38**, 389–395.
8 T. Li, Q. Fan, T. Liu, X. L. Zhu, J. Zhao and G. X. Li, *Biosens. Bioelectron.*, 2010, **25**, 2686–2689.
9 R. M. Wang, J. Di, J. Ma and Z. F. Ma, *Electrochim. Acta*, 2012, **61**, 179–184.
10 K. A. Foon and R. F. Todd, *Blood*, 1986, **68**, 1–31.
11 J. Whangpeng and T. Knutsen, *Clin. Haematol.*, 1980, **9**, 87–127.
12 B. Lowenberg, J. R. Downing and A. Burnett, *N. Engl. J. Med.*, 1999, **341**, 1051–1062.
13 C. H. Pui and W. E. Evans, *N. Engl. J. Med.*, 1998, **339**, 605–615.
14 http://www.cancer.org/acs/groups/cid/documents/webcontent/003054-pdf.pdf, accessed on 05 February 2013.
15 http://www.cancer.org/acs/groups/cid/documents/webcontent/003110-pdf.pdf, accessed on 05 February 2013.
16 S. Faderl, H. M. Kantarjian, M. Talpaz and Z. Estrov, *Blood*, 1998, **91**, 3995–4019.
17 G. Juliusson and J. Liliemark, *J. Clin. Oncol.*, 1993, **11**, 679–689.
18 J. Muhlmann, J. Thaler, W. Hilbe, O. Bechter, M. Erdel, G. Utermann and H. C. Duba, *Genes, Chromosomes Cancer*, 1998, **21**, 90–100.
19 G. P. Browman, P. B. Neame and P. Soamboonsrup, *Blood*, 1986, **68**, 900–905.
20 V. Buccheri, V. Shetty, N. Yoshida, R. Morilla, E. Matutes and D. Catovsky, *Br. J. Haematol.*, 1992, **80**, 62–68.
21 D. S. Gordon, J. J. Hutton, R. V. Smalley, L. M. Meyer and W. R. Vogler, *Blood*, 1978, **52**, 1079–1088.
22 R. Paredes-Aguilera, L. Romero-Guzman, N. Lopez-Santiago, L. Burbano-Ceron, O. Camacho-Del Monte and S. Nieto-Martinez, *Am. J. Hematol.*, 2001, **68**, 69–74.
23 L. W. Diamond, B. N. Nathwani and H. Rappaport, *Cancer*, 1982, **50**, 1122–1135.
24 A. Guerci, J. L. Merlin, N. Missoum, L. Feldmann, S. Marchal, F. Witz, C. Rose and O. Guerci, *Blood*, 1995, **85**, 2147–2153.
25 F. Lacombe, F. Durrieu, A. Briais, P. Dumain, F. Belloc, E. Bascans, J. Reiffers, M. R. Boisseau and P. Bernard, *Leukemia*, 1997, **11**, 1878–1886.
26 L. Belov, O. de la Vega, C. G. dos Remedios, S. P. Mulligan and R. I. Christopherson, *Cancer Res.*, 2001, **61**, 4483–4489.

27 M. Dugas, C. Schoch, S. Schnittger, T. Haferlach, S. Danhauser-Ried, W. Hiddemann, D. Messerer and K. Uberla, *Leukemia*, 2001, **15**, 1805–1810.
28 M. J. Pongers-Willemse, O. Verhagen, G. J. M. Tibbe, A. J. M. Wijkhuijs, V. de Haas, E. Roovers, C. E. van der Schoot and J. J. M. van Dongen, *Leukemia*, 1998, **12**, 2006–2014.
29 J. Borrow, A. D. Goddard, B. Gibbons, F. Katz, D. Swirsky, T. Fioretos, I. Dube, D. A. Winfield, J. Kingston, A. Hagemeijer, J. K. H. Rees, T. A. Lister and E. Solomon, *Br. J. Haematol.*, 1992, **82**, 529–540.
30 T. Flohr, A. Schrauder, G. Cazzaniga, R. Panzer-Grumayer, V. van der Velden, S. Fischer, M. Stanulla, G. Basso, F. K. Niggli, B. W. Schafer, R. Sutton, R. Koehler, M. Zimmermann, M. G. Valsecchi, H. Gadner, G. Masera, M. Schrappe, J. J. M. van Dongen, A. Biondi, C. R. Bartram and B. S. I, *Leukemia*, 2008, **22**, 771–782.
31 J. J. M. van Dongen, E. A. Macintyre, J. A. Gabert, E. Delabesse, V. Rossi, G. Saglio, E. Gottardi, A. Rambaldi, G. Dotti, F. Griesinger, A. Parreira, P. Gameiro, M. G. Diaz, M. Malec, A. W. Langerak, J. F. San Miguel and A. Biondi, *Leukemia*, 1999, **13**, 1901–1928.
32 R. A. Ghossein and S. Bhattacharya, *Eur. J. Cancer*, 2000, **36**, 1681–1694.
33 Q. H. Min, R. A. Wu, L. A. Zhao, H. Q. Qin, M. L. Ye, J. J. Zhu and H. F. Zou, *Chem. Commun.*, 2010, **46**, 6144–6146.
34 S. S. Zhang, H. Zhong and C. F. Ding, *Anal. Chem.*, 2008, **80**, 7206–7212.
35 T. T. Zheng, J. J. Fu, L. H. Hu, F. Qiu, M. Hu, J. J. Zhu, Z. C. Hua and H. Wang, *Anal. Chem.*, 2013, **85**, 5609–5616.
36 K. Sefah, Z. W. Tang, D. H. Shangguan, H. Chen, D. Lopez-Colon, Y. Li, P. Parekh, J. Martin, L. Meng, J. A. Phillips, Y. M. Kim and W. H. Tan, *Leukemia*, 2009, **23**, 235–244.
37 Y. F. Huang, D. H. Shangguan, H. P. Liu, J. A. Phillips, X. L. Zhang, Y. Chen and W. H. Tan, *ChemBioChem*, 2009, **10**, 862–868.
38 T. Chu, J. Ebright and A. D. Ellington, *Curr. Opin. Mol. Ther.*, 2007, **9**, 137–144.
39 W. H. Thiel, T. Bair, A. S. Peek, X. Y. Liu, J. Dassie, K. R. Stockdale, M. A. Behlke, F. J. Miller and P. H. Giangrande, *PLoS One*, 2012, **7**, e43836.
40 L. Yang, L. Meng, X. B. Zhang, Y. Chen, G. Z. Zhu, H. P. Liu, X. L. Xiong, K. Sefah and W. H. Tan, *J. Am. Chem. Soc.*, 2011, **133**, 13380–13386.
41 D. Y. Zhao, J. L. Feng, Q. S. Huo, N. Melosh, G. H. Fredrickson, B. F. Chmelka and G. D. Stucky, *Science*, 1998, **279**, 548–552.
42 R. Cui, C. Liu, J. Shen, D. Gao, J.-J. Zhu and H.-Y. Chen, *Adv. Funct. Mater.*, 2008, **18**, 2197–2204.
43 B. P. Nelson, R. Candal, R. M. Corn and M. A. Anderson, *Langmuir*, 2000, **16**, 6094–6101.
44 C. B. Liu, K. Wang, S. L. Luo, Y. H. Tang and L. Y. Chen, *Small*, 2011, **7**, 1203–1206.
45 L. Y. Chen, Y. H. Tang, K. Wang, C. B. Liu and S. L. Luo, *Electrochem. Commun.*, 2011, **13**, 133–137.
46 D. Li, M. B. Mueller, S. Gilje, R. B. Kaner and G. G. Wallace, *Nat. Nanotechnol.*, 2008, **3**, 101–105.
47 Y. Xu, H. Bai, G. Lu, C. Li and G. Shi, *J. Am. Chem. Soc.*, 2008, **130**, 5856–5857.
48 J. J. Zhang, M. M. Gu, T. T. Zheng and J. J. Zhu, *Anal. Chem.*, 2009, **81**, 6641–6648.
49 T. T. Zheng, R. Zhang, L. F. Zou and J. J. Zhu, *Analyst*, 2012, **137**, 1316–1318.
50 O. C. Farokhzad, J. J. Cheng, B. A. Teply, I. Sherifi, S. Jon, P. W. Kantoff, J. P. Richie and R. Langer, *Proc. Natl. Acad. Sci. U. S. A.*, 2006, **103**, 6315–6320.
51 O. C. Farokhzad, S. Y. Jon, A. Khademhosseini, T. N. T. Tran, D. A. LaVan and R. Langer, *Cancer Res.*, 2004, **64**, 7668–7672.
52 D. Shangguan, Y. Li, Z. W. Tang, Z. H. C. Cao, H. W. Chen, P. Mallikaratchy, K. Sefah, C. Y. J. Yang and W. H. Tan, *Proc. Natl. Acad. Sci. U. S. A.*, 2006, **103**, 11838–11843.

